International Forum on Aeroelasticity and Structural Dynamics
IFASD 2019
9-13 June 2019, Savannah, Georgia, USA

INFLUENCE ON THE FLUTTER BEHAVIOR OF PRE-STRESSED WING STRUCTURES UNDER AERODYNAMIC LOADING

Andreas Hermanutz[1] **and Mirko Hornung**[1]

[1]Technical University of Munich, Institute of Aircraft Design
andreas.hermanutz@tum.de, mirko.hornung@tum.de

Keywords: Computational aeroelasticity, flutter prediction, high aspect ratio flexible wing

Abstract: Modern wing designs exhibit a significant increase in wing flexibility through slenderer wings in combination with an extensive lightweight structural design. Especially wing flutter becomes increasingly important with higher elasticity. In addition, wings with increased elasticity show a significantly higher deflection between jig- and flight-shape. For this purpose, the effects of changes in stiffness, mass matrix and different lift distributions between jig and 1g trimmed cruise condition are analyzed with regard to the flutter prediction according to the p-k method. The structural and aerodynamic effects are exemplary compared using a generic composite higher aspect ratio swept wing, where the most significant influence could be identified by the simple geometrical change from jig- to flight-shape.

1 INTRODUCTION

The development of innovative aircraft that are more environment-friendly, safer and cheaper are essential objectives of aerospace research. The continuous improvement of the efficiency can be done by modifications such as the use of new materials, optimisations in aerodynamics and structural design [1]. Small modifications are ensuring lower development cost as well as risk minimisations, compared to a complete new system. On the other hand, the scope for improvement is limited for small changes.

The development of wings with higher aspect ratios for transport aircraft has the potential to reduce induced drag and thus increase aircraft operational efficiency. Therefore in different works, such as e.g. [2] [3], the accurate prediction and suppression of flutter is investigated. The increased aspect ratio leads to a small wing chord. Thus the wings are more slender and exhibit a significant increase in wing flexibility, which is further enhanced by an extensive lightweight structural design.

Increasing wing flexibility inherently leads to more aeroelastic effects, for which accurate methods of prediction are essential throughout the development process. In Palacios et al. [4] the most important effects on highly flexible wings are discussed, especially the influence of geometric nonlinearities due to large deformations. Usually, the structural engineers are working with the wings jig-shape, as this represents the unloaded reference condition. To optimize the wings aerodynamics, aerodynamic engineers typically work with the wings flight-shape. Thus, creating a consistent aeroelastic model requires adapting one model to the other. Since the predesigned aerodynamic flight-shape is typically a target design depending on the flexibility of the wing, it is more reasonable to proceed from a coupled aeroelastic model in jig-shape, as e.g. presented in [5].

To describe the structural dynamics, it is convenient to transform stiffness and mass matrix, based on the jig-shape wing structure, into modal coordinates. Compared to stationary cruise flight, the changes in aerodynamic loads caused by wing bending and torsion are not taken into account. In addition, pre-stressed structures show a natural change in their dynamic behavior, due to changes in the stiffness matrix. These modifications are caused by simple geometric changes due to large deformation and stress-stiffening effects caused by the internal structural load. Consequently, as described in [4] [6] an update is required depending on the pre-loaded wing shape. In this study those influences on the calculation of the critical flutter pressure based on the p-k method are investigated.

2 THEORY AND COMPUTATIONAL METHODS

The starting point of this work is the continuum mechanical description for the fluid and the structural field. Both are considered separately from each other and solvers optimized for each individual problem are used. Therefore, a staggered coupling approach is selected for the fluid-structure-interaction simulation [7].

The structure is described in the Lagrange formulation according to Equation 1 [8]. In this context, $\bar{\bar{S}}$ is the 2nd Piola-Kirchhoff stress tensor, $\bar{\bar{F}}$ the deformation gradient, $\bar{b}$ the volume force vector, ρ the material density and $\bar{u}$ the structural displacement field. To solve the differential equation for the displacement $\bar{u}$, the Finite Element Method (FEM) is used as calculation method, which can generally be rewritten in matrix notation as a system of linear equations according to Equation 2,

$$div(\bar{\bar{F}} \cdot \bar{\bar{S}}) + \rho\bar{b} = \rho\frac{\partial^2}{\partial t^2}\bar{u} \qquad (1)$$

$$\bar{M}\ddot{\bar{u}} + \bar{B}\dot{\bar{u}} + \bar{K}\bar{u} = \bar{F} \qquad (2)$$

where $\bar{K}$ stands for the stiffness, $\bar{M}$ for the mass and $\bar{B}$ for the structual damping matrix. Taking into account nonlinear effects, the stiffness matrix and force vector $\bar{F}$ are further dependent on the displacement $\bar{u}$, which leads to a system of nonlinear equations. The nonlinear description of the structure allows all relevant structural nonlinearities to be covered, the most important being the one due to large deformations. The tracking of the surface normals, which indirectly describes the change in the direction of the force, is an essential requirement for the fluid-structure-interaction simulation.

The fluid flow is modeled with the arbitrary Lagrangian-Eulerian formulation of the Reynolds-Averaged compressible Navier-Stoke equations (RANS) without volume forces. The fluid air is being treated as an ideal gas. The flow domain is discretization with the finite-volume method and the resulting nonlinear system of equations solved with a pressure-based coupled algorithm. Since not all turbulence cascades are resolved, the RANS equations are used in combination with the Spalart-Allmaras turbulence model [9].

In order to perform the Fluid-Structure-Interaction (FSI) simulation, the interface forces $\bar{F}_I$ and the displacement $\bar{u}_I$ must be transferred across the nonconforming interfaces. Hence, a method for calculating a mapping matrix $\bar{A}$ is required. A possible way of doing this is described in [10]. Once $\bar{A}$ is available, for none sliding interface meshes, the data can be transferred according to Equation 3 and Equation 4. The additional mapping matrix $\bar{E}$ is used to map the cell-centered pressure force data to node-based forces.

$$\bar{u}_{CFD} = \bar{A} \cdot \bar{u}_{CSM} \quad (3) \qquad \bar{F}_{CSM} = \bar{A}^T \cdot \bar{E} \cdot \bar{F}_{CFD} \quad (4)$$

The fluid domain does not undergo any topological changes, but with the moving interface the interior cells have to be modified. The position of the updated cell nodes is determined by solving the diffusion equation with a cell position dependent diffusion parameter.

2.1 Equation of Aeroelasticity

The structural dynamics of the flexible aircraft in terms of physical coordinates is described by Equation 2. To reduce the complexity of the model, it is useful to reduce the system complexity by transferring it to generalized coordinates. With the eigenvector matrix $\bar{\Phi}$, Equation 2 can be rewritten in the following way:

$$\bar{M}_{gen}\ddot{q} + \bar{B}_{gen}\dot{q} + \bar{K}_{gen}q = \bar{F}_{gen} \quad (5)$$

where $\bar{M}_{gen}$, $\bar{B}_{gen}$ and $\bar{K}_{gen}$ represent the diagonal matrix of the generalized mass, damping and stiffness matrix [11]. The vector of the generalized aerodynamic forces $\bar{F}_{gen}$ is computed in the context of this work by the use of CFD simulations. For the present work, Equation 5 is transferred to the frequency domain. The generalized aerodynamic force matrix $\bar{Q}_{hh}(Ma, k_{red})$ is determined from the harmonic response of the wing [12]. Together with the angular frequency ω and the generalized aerodynamic force matrix $\bar{Q}_{hh}(Ma, k_{red})$, the well-known flutter equation can be formulated as follows

$$[-\omega^2 \bar{M}_{gen} + \bar{K}_{gen} - \frac{\rho \cdot U_\infty^2}{2} \bar{Q}_{hh}(Ma, k_{red})]q_0 = 0 \quad (6)$$

With the mean aerodynamic chord c_m, and the free stream velocity U_∞, the reduced frequency k_{red} is given as follows

$$k_{red} = \frac{\omega \cdot c_m}{2 \cdot U_\infty} \quad (7)$$

To evaluate the critical condition where the structural motion is getting unstable, the p-k flutter method in state-space formulation, as presented in [13], is used. In order to solve Equation 6, a continuous progression of the transient aerodynamic forces, depending on k_{red}, is required. For this, a discrete number of reduced frequencies is calculated. Further values for k_{red} are computed using a linear interpolation.

2.2 Aeroelastic Framework and Simulation Approach

The present work is based on the aeroelastic framework *ceas++* [14], which is a development environment for high fidelity computational aeroelastic simulations. The core elements are code adapters for commercial CSM and CFD solvers as well as an inverse shape mapping algorithm for data transmission over non-conforming interface meshes. With full access to the staggered coupling process of the fluid-structure-interaction simulation, a high capability for individualized algorithms is given.

Since the wing flight-shape is required for the presented work, the aircraft is brought into a stable 1g trimmed level flight condition. The method used to determined the equilibrium state is described in [14]. In this paper the framework was extended by the possibility to calculate the generalized aerodynamic forces $\bar{Q}_{hh}$ for an arbitrary flight conditions based on CFD methods. Additionally, the p-k flutter method was implemented to predict the critical flight conditions. In order to investigate the most important physical influences, three different case studies were carried out. In the first basic study, the critical flutter pressure is determined in the wing's jig-shape. Herefore, the eigenmode matrix $\bar{\Phi}$ is calculated and the generalize mass and stiffness matrix exported. The eigenmodes, scaled to an amplitude of $1/500 \cdot c_m$ as suggested in [15], are used to calculate the unsteady aerodynamic forces. The time domain solution is then converted to modal coordinates and finally transformed into the frequency domain.

In the second study, first a trim calculation is undertaken. Based on the changed global AoA and the resulting aerodynamic forces, the wings structural and aerodynamic model is updated to the flight-shape. In order to investigate the pure geometrical flight-shape influences, structural pre-loading and thus stress-stiffening effects are not considered. Hence, the load history is not considered and the stiffness and mass matrix based on the updated mesh coordinates are re-integrated and re-assembled. In strict sense, mass conservation is not fulfilled in this approach. This would require an update of the element density, but since the elements strains are small and the total mass deviation of the wing between jig- and flight-shape is less than $\Delta m/MTOW < 0.0076\%$, this is neglected. With the updated models, the aeroelastic model is constructed, as explained in the first study.

In study three, additional changes in the stiffness matrix caused by the pre-loaded state are taken into account. The simulation concept follows the second study, with the exception that the load history is used to obtain the stiffness and mass matrix in the flight-shape. The principal simulation approach for all three studies is sketched in Figure 1.

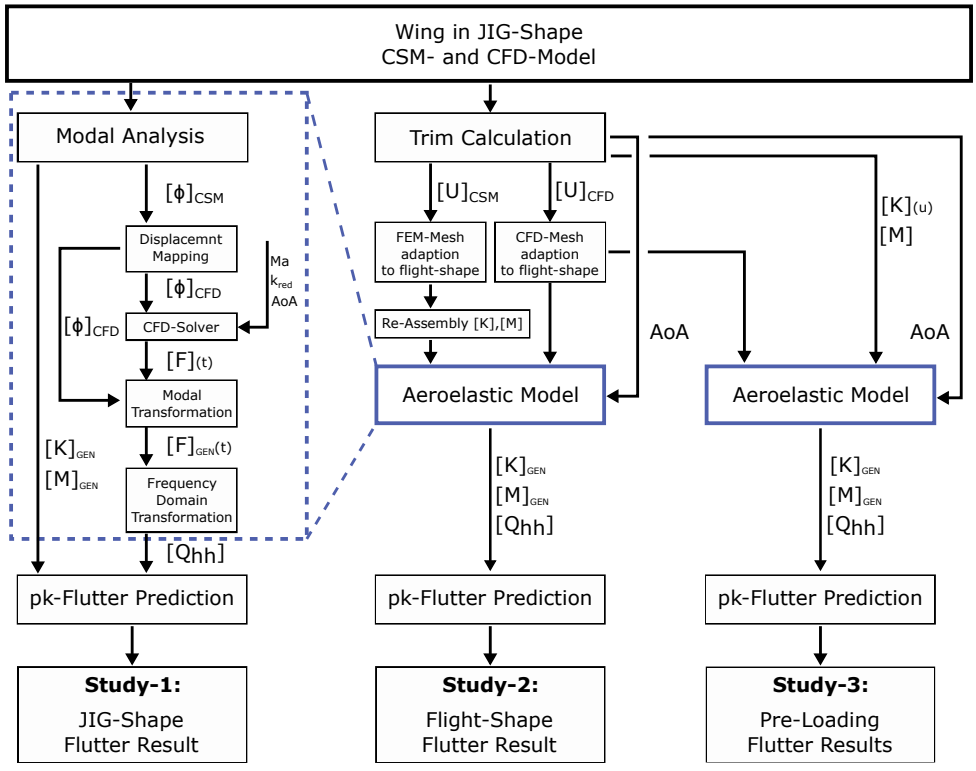

Figure 1: Simulation approach.

3 COMPUTATIONAL MODELS FOR THE ELASTIC WING CASE STUDY

A swept wing of a generic transport aircraft with high aspect ratio, as shown in Figure 2, is used as a demonstration example. For the following study a MTOW of 102t is used. The basic parameters of the wing plan form are shown in Table 1. In order to set up the methodological process and to reduce computational effort, the study is limited to the wing half model. For this reason, only symmetric flight conditions and wing motions are possible. Antisymmetric modes are important to describe the overall physical behavior of aircraft motion, but have not been considered for this study.

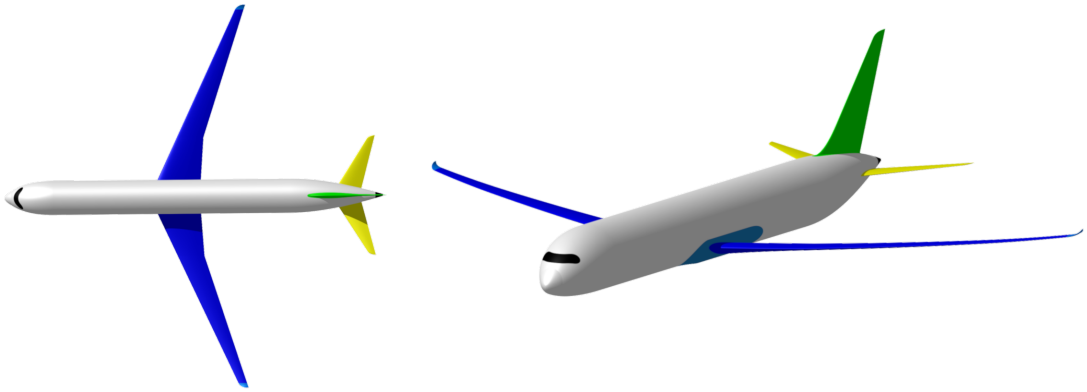

Figure 2: Generic flexible wing aircraft configuration.

Table 1: Wing planform parameters.

Wing Area (S)	Aspect Ratio (AR)	Taper Ratio (TR)	Wing Sweep (Λ)
$158\,\mathrm{m}^2$	14.0	0.2	$25\,\mathrm{deg}$

3.1 Structural Wing Model

Due to their high lightweight potential, modern composite materials are used in structural wing design. The FE method with shell element discretization is used as structural model. For overlapping areas like stringer or spar flanges, a smeared stiffness approach is used. The anisotropic stiffness behavior of the shell elements is described by classical laminate theory. The complete wetted area of the wing is used for the FSI simulation. For this reason, a representation of the leading and trailing edge devices of the wing, capable of dealing with the FSI interface variables, is required. A simple sandwich construction is used for this, which is also represented by shell elements. In order to avoid artificial stiffening of the wing box, the individual DoFs of the flap surfaces, with the exception of the joints, are decoupled. To model the aircraft mass, the wing structural weight is calculated using a density-based approach. As shown in Figure 3, engine, fuel and fuselage, including sub-components and payload, are modeled with discrete mass points.

In order to adapt the FE model to the flight-shape, it is also required to consider the change of the local direction of the material coordinate systems. This is done via an additional coordinate system model that uses fixed reference points on the wing, instead of fixed coordinates. Thus, the material orientation can easily be updated with the resulting displacement results of the wing.

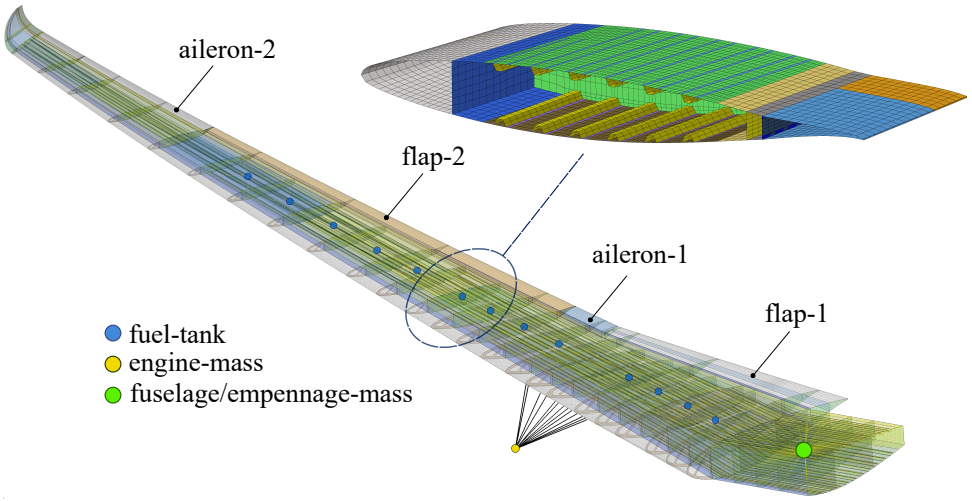

Figure 3: Structural finite element wing model.

3.2 Aerodynamic Wing Model

The steady and unsteady aerodynamic forces are calculated using CFD methods, solving the compressible RANS equations. A finite volume pressure based solver is used for this purpose. Spalart-Allmaras with additional wall function correction is used as turbulence model. The flow domain, shown in Figure 4, is discretized with hex dominated cells. Normal forces are of major interest, while the computing effort is kept as low as possible. Therefore, the number of cells is reduced to 12.0 million. If aerodynamic drag is a particular focus in aerodynamic efficiency assessment, the computational grid must meet much higher accuracy requirements. Further, the aerodynamic influence of an engine is not considered and therefore not present in the aerodynamic model.

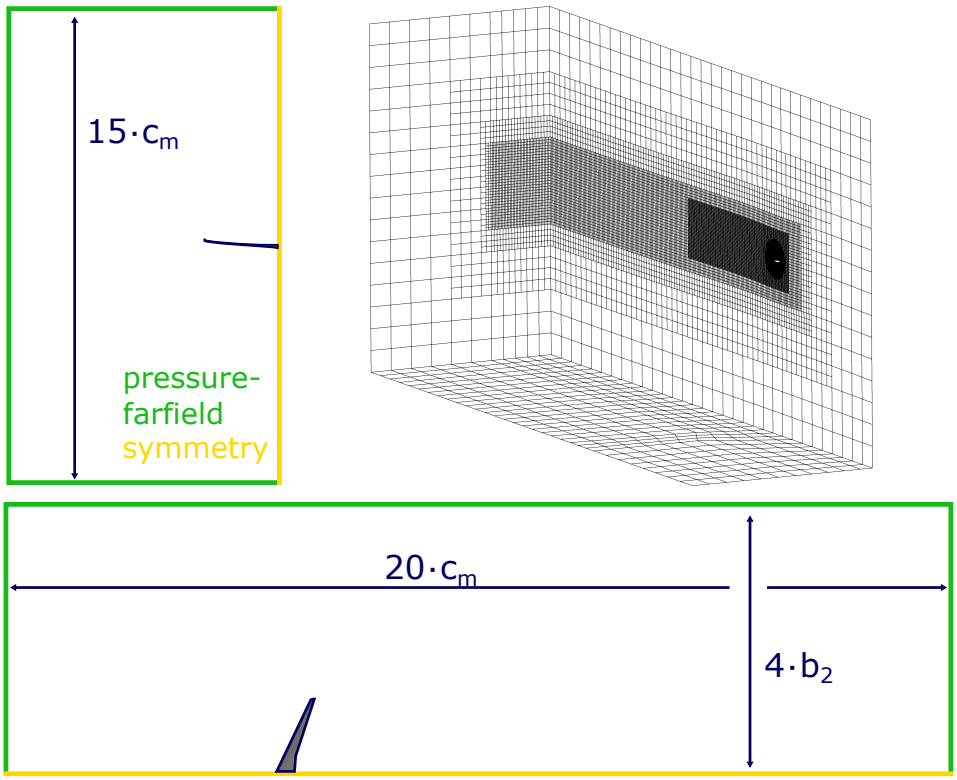

Figure 4: Computational aerodynamic domain and discretized half model.

4 SIMULATION RESULTS

The case study is carried out with a cruise Mach number of $Ma = 0.8$ at flight level $FL = 330$. The necessary angle of attack (AoA) α is determined for a load factor of $1g$ for a quasi-stationary level flight condition. The resulting flight shape at $\alpha = 0.268\,\mathrm{deg}$ is shown in Figure 5. The trim results are computed as presented in [14].

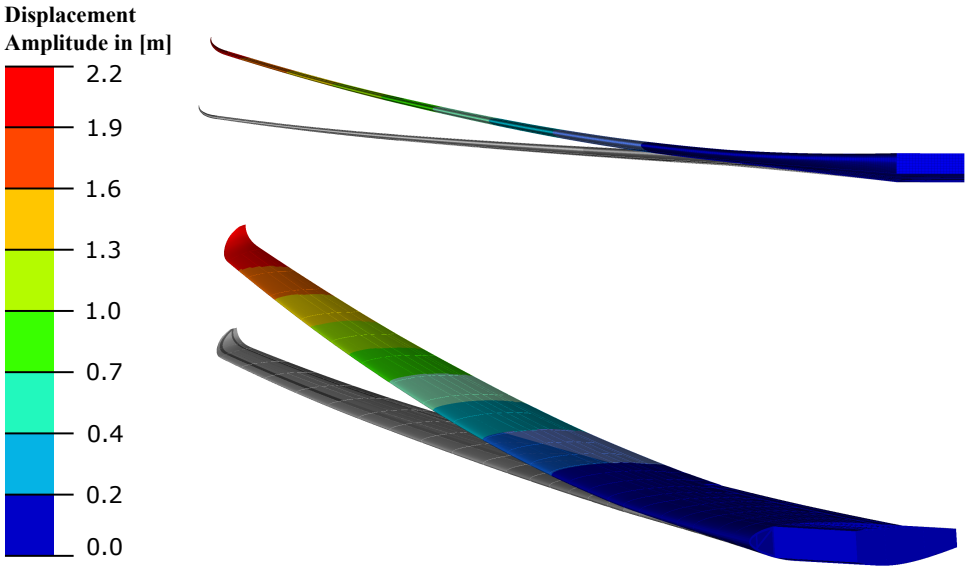

Figure 5: Wing deformation at $1g$ quasi-steady trimmed level flight condition at $Ma = 0.8$, $FL = 330$.

4.1 Structural Dynamics Influences

The eigenmodes of the aircraft wing are calculated with the Lanczos algorithm, as implemented in MSC NASTRAN [16]. For the presented study ten elastic eigenmodes, as shown in Figure 6, are taken into account to describe the structural dynamics. The rigid-body dynamics of the aircraft have been neglected.

To evaluate the changes in modal stiffness, mass and frequency, the resulting $1g$ static flight loads are scaled with the parameter λ and incrementally applied to the wing. Variations for each mode are plotted in Figure 7. One can see that not all modes are influenced by the pre-load with the same intensity. The bending dominated mode-3 and torsional mode-9 show the largest changes in modal properties. Except for mode-9 the natural frequencies of the wing, which are directly dependent on the modal stiffness and mass, tend to decrease in comparison to the jig-shape. Mode-9 and mode-3 shows further a significant nonlinear behaviour depending from the loading, what can be explained with the changed mode shapes.

The change in the modal stiffness and mass between the flight-shape and pre-loaded wing model is shown in Table 2. Only small changes can be observed, which is why it is not possible to say whether the deviation is caused by the pre-loading or numerical variations in the material coordinate system model. To increase the stress-stiffening effect, the load is additionally scaled to $\lambda = 1.5$. It can be seen that the influences on the modal mass and stiffness matrix are increased. To see a larger influences, higher load factors are necessary, what is due to buckling not arbitrary possible. For the flight condition with a load factor of 1g, it can be summarized that no significant changes are recognizable.

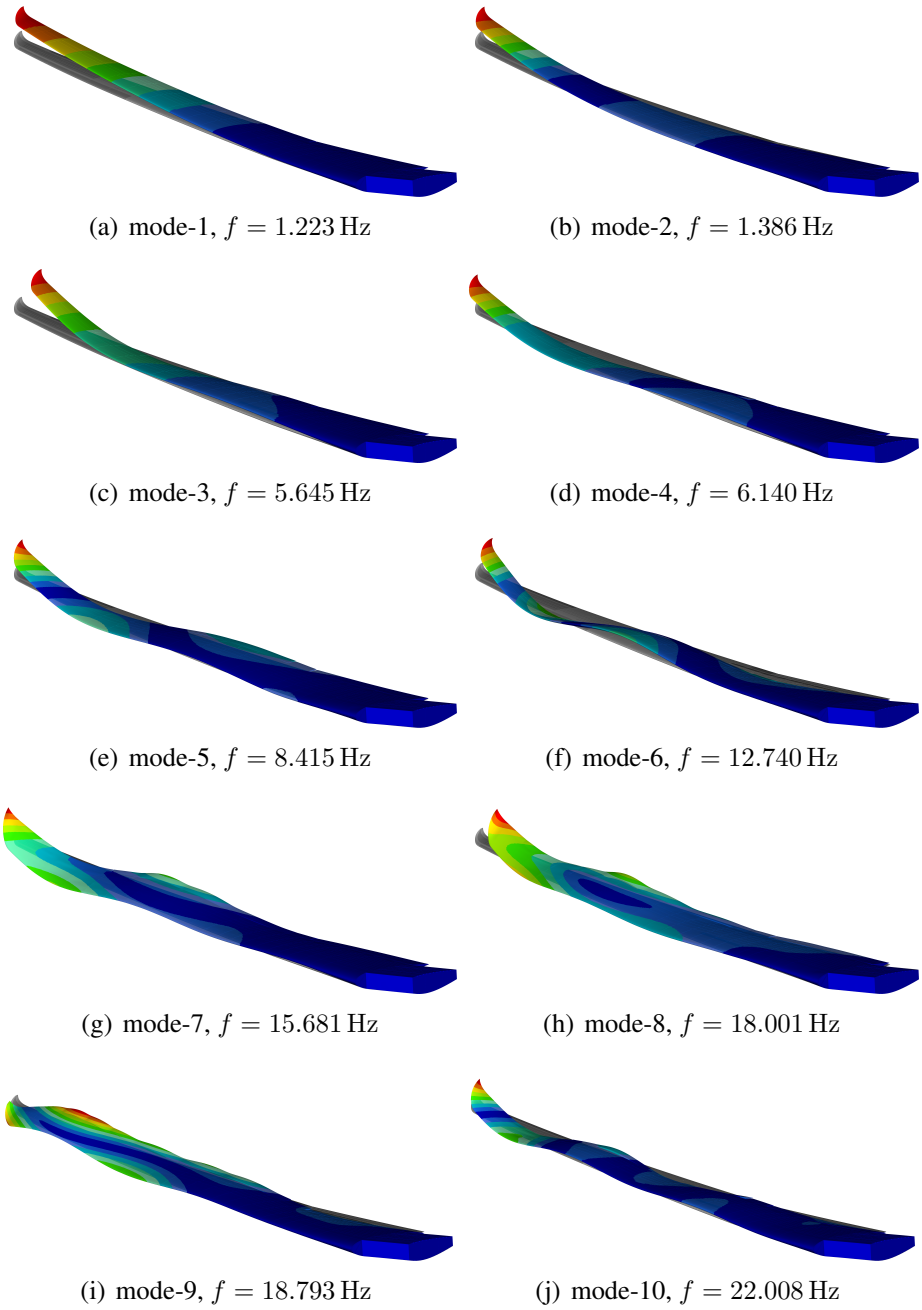

(a) mode-1, $f = 1.223\,\mathrm{Hz}$ (b) mode-2, $f = 1.386\,\mathrm{Hz}$

(c) mode-3, $f = 5.645\,\mathrm{Hz}$ (d) mode-4, $f = 6.140\,\mathrm{Hz}$

(e) mode-5, $f = 8.415\,\mathrm{Hz}$ (f) mode-6, $f = 12.740\,\mathrm{Hz}$

(g) mode-7, $f = 15.681\,\mathrm{Hz}$ (h) mode-8, $f = 18.001\,\mathrm{Hz}$

(i) mode-9, $f = 18.793\,\mathrm{Hz}$ (j) mode-10, $f = 22.008\,\mathrm{Hz}$

Figure 6: First ten structural jig-shape eigenmodes. Displacement values scaled to $|\delta u| = 1\,\mathrm{m}$

The modal assurance criterion (MAC) according to Equation 8 is used to identify variations in the mode shapes. The displacement vectors are compared to each other in jig- and flight-shape, as well for the unloaded and pre-loaded wing structure in flight-shape. The results are presented in Table 3.

$$MAC(\bar{u}_1, \bar{u}_2) = \frac{|\bar{u}_1^T \bar{u}_2|^2}{|\bar{u}_1||\bar{u}_2|} \tag{8}$$

Except for mode-8 and mode-9, only small changes between jig- and flight-shape can be observed. The low MAC value for mode-9 continues to be an identification of the high nonlinear

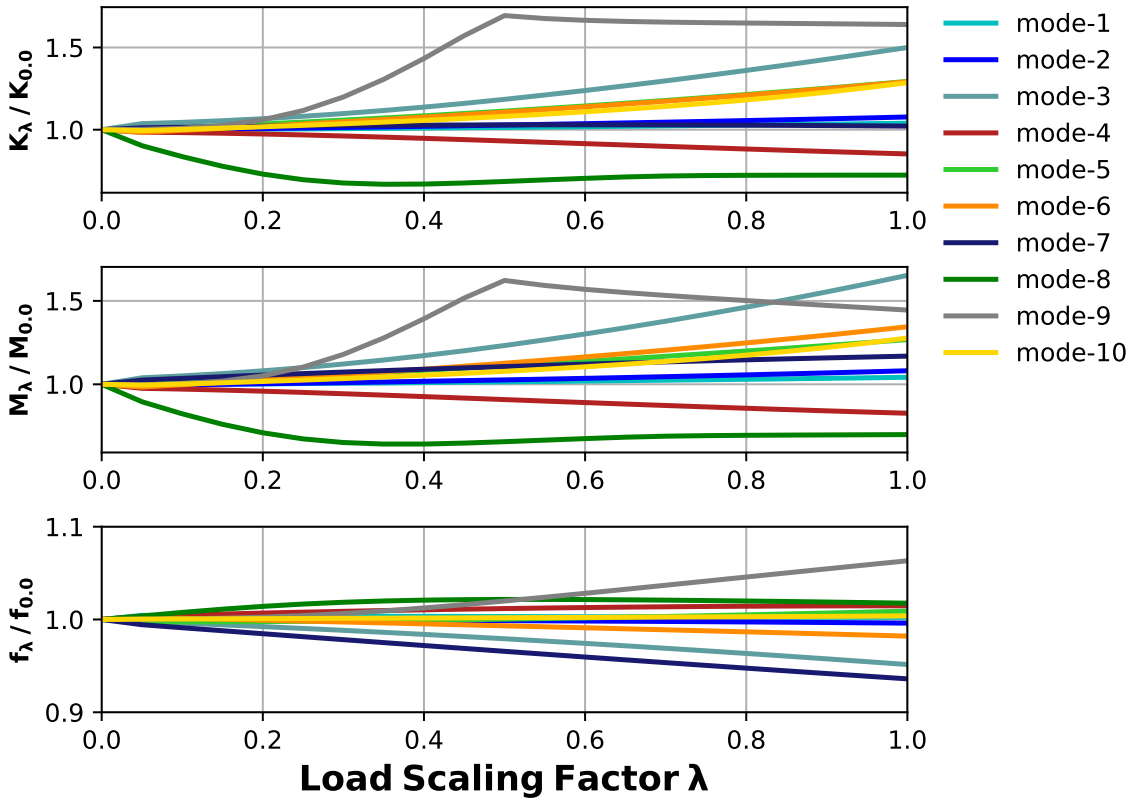

Figure 7: Eigenfrequency changes depending from external structural loading.

Table 2: Changes in mass and stiffness matrix due to pre-loading effect. $\Delta\% = |\Delta K_{gen}|/K_{gen}$

$\lambda = 1.0$	**mode-1**	**mode-2**	**mode-3**	**mode-4**	**mode-5**
ΔM_{gen}:	0.06%	0.14%	0.90%	0.20%	0.08%
ΔK_{gen}:	0.38%	0.03%	0.36%	0.08%	0.02%
	mode-6	**mode-7**	**mode-8**	**mode-9**	**mode-10**
ΔM_{gen}:	1.62%	1.59%	0.27%	2.96%	1.20%
ΔK_{gen}:	1.29%	2.04%	0.24%	2.99%	1.28%
$\lambda = 1.5$	**mode-1**	**mode-2**	**mode-3**	**mode-4**	**mode-5**
ΔM_{gen}:	0.84%	12.84%	1.14%	12.21%	14.62%
ΔK_{gen}:	9.47%	8.54%	5.05%	16.35%	13.04%
	mode-6	**mode-7**	**mode-8**	**mode-9**	**mode-10**
ΔM_{gen}:	13.34%	3.30%	0.42%	5.10%	37.60%
ΔK_{gen}:	11.37%	0.15%	3.00%	3.88%	37.71%

Table 3: MAC value results of eigenmode shapes comparison.

structural mode	**1**	**2**	**3**	**4**	**5**	**6**	**7**	**8**	**9**	**10**
jig- to flight-shape	0.987	0.975	0.972	0.976	0.968	0.951	0.980	0.484	0.100	0.962
flight-shape to pre-loaded wing	1.0	0.999	0.999	0.998	0.999	0.999	0.998	0.999	0.998	0.999

response of the modal stiffness and mass at $\lambda = 0.5$ in Figure 7. As those are projections onto the eigenmodes, it is plausible that a step is to be expected as soon as a mode changes. A direct

comparison of the displacement field for mode-8 and mode-9 is illustrated in Figure 8.

In the case of the flight shape modes compared to the pre-stressed structure modes, it can be observed that all MAC values are close to $MAC \approx 1.0$. That means, that there is no relevant change in the present mode shape. Considering the results shown in Figure 7, only the changed geometrical influences will influence the modal stiffness and mass and are thus included in Equation 6. The similarity of the eigenmodes means in addition, that the matrix of generalized aerodynamic forces does not show any differences between the unloaded and pre-loaded wing in flight-shape. For the application, this is a relevant insight, because no additional computation effort is necessary to obtain a new set of unsteady aerodynamic forces to assemble the $\bar{Q}_{hh}$ matrix.

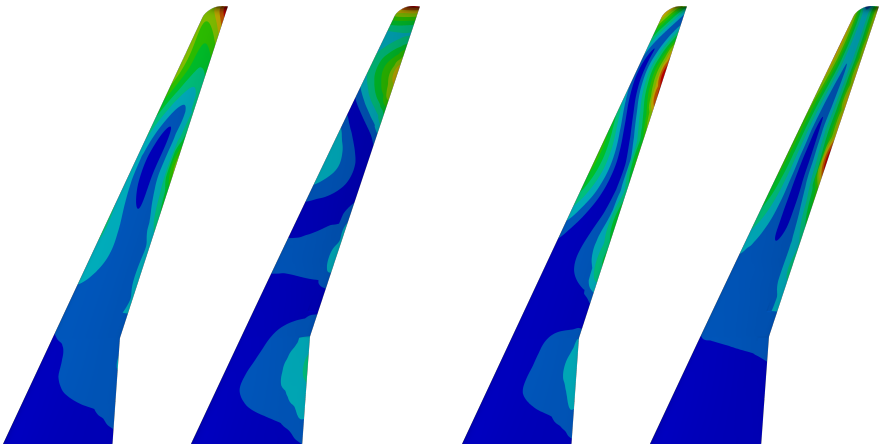

(a) mode-8, jig-shape (left), flight-shape (right)

(b) mode-9, jig-shape (left), flight-shape (right)

Figure 8: Differences of the wing eigenmode shapes.

4.2 Aerodynamic Influences

In addition to the structural dynamics, changes in wing aerodynamics have also been included and initially observed individually. The pressure distribution between jig- and flight-shape is shown in Figure 9. As can be seen, the intensity of the shock decreases in the outer wing area. The reason for this is the reduced local AoA, which is caused by the wing washout effect, which is typical for elastic swept wings. Between jig- and flight-shape distribution, it has also to be considered that the flight-shape is in a trimmed flight condition, such that the global AoA is not zero. A considerable change in the lift distribution can be observed, which also affects the unsteady aerodynamic forces.

In the following section, the structural and aerodynamic effects will be analyzed together with respect to the flutter prediction.

4.3 Aeroelastic Flutter Results

The set of ten structural eigenmodes is used to calculate the unsteady aerodynamic forces, which are evaluated for $k_{red} = [0.0, 0.05, 0.2, 0.8, 2.0, 3.0]$. The flutter equation is solved with the p-k method for a dynamic pressure range q_∞ from $0.5\,\mathrm{kPa}$ to $42.0\,\mathrm{kPa}$. Structural damping is not considered.

The flutter analysis results in two unstable modes for the jig-shape study. For the studies with the wing in flight-shape, only one unstable mode can be identified. The corresponding root

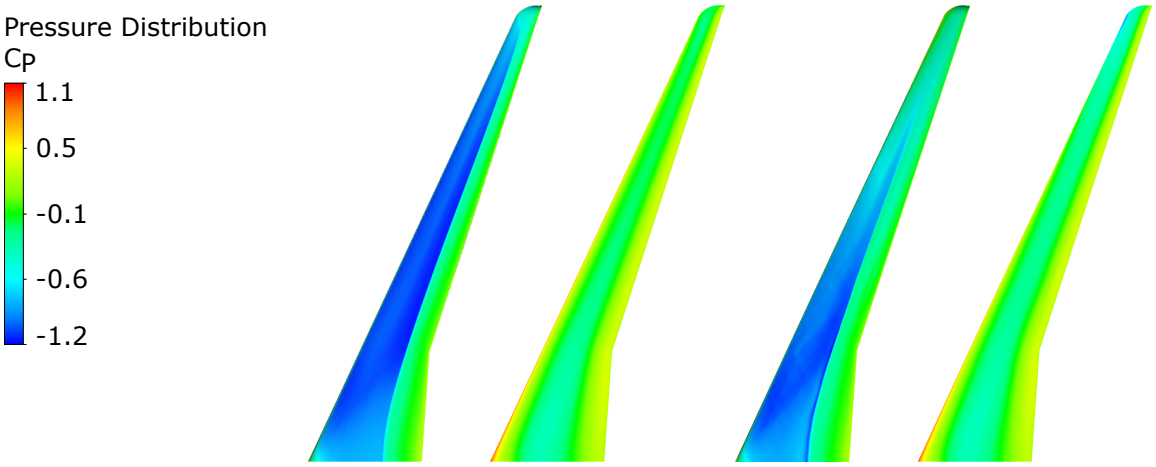

(a) jig-shape (b) flight-shape

Figure 9: Wing pressure distribution of jig- and flight-shape at steady flow state, upper surface (left), lower surface (right)

locus plots are shown in Figure 10. In all three cases, mode-3 becomes unstable. For the wing in jig-shape, mode-4 becomes additionally unstable. It can also be seen that there are no significant influences between the geometrical flight-shape configuration and the pre-loaded wing structure. This is in accordance with the previous results. In addition, the frequency and damping trends over the dynamic pressure q_∞ at $Ma = 0.8$ are presented in Figure 11. As in the root locus diagram, the pre-loaded wing shows no significant difference to the flight-shape, which is why the damping and frequency results are not plotted for the purposes of clarity. The resulting flutter boundaries for all three cases are summarized in Table 4.

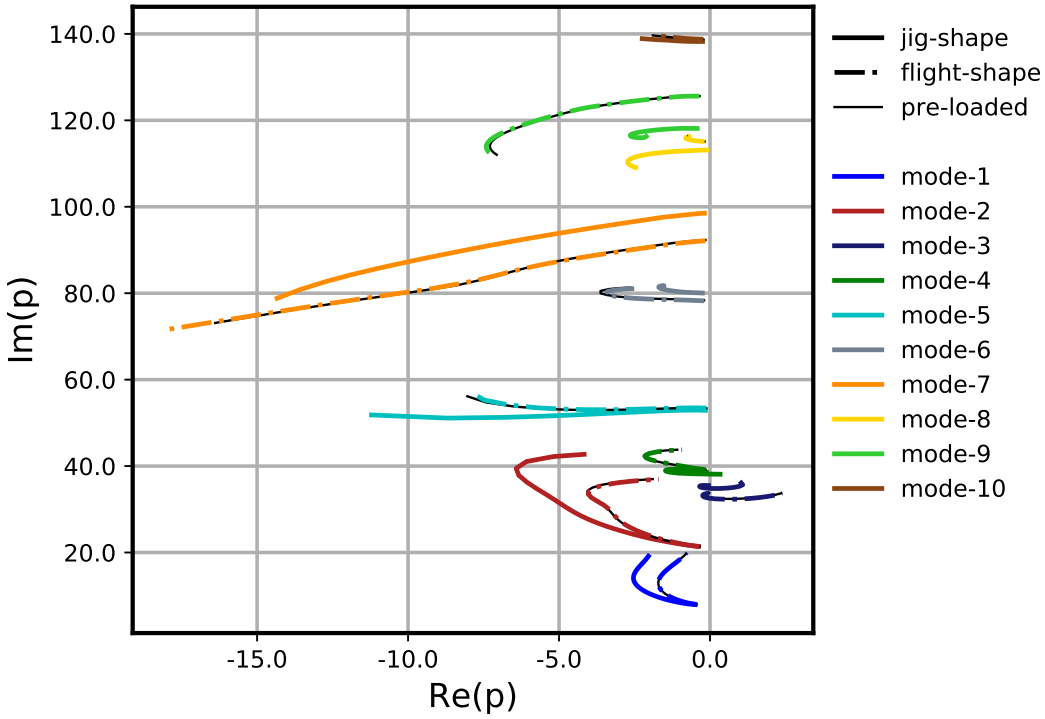

Figure 10: Root locus of the three case studies.

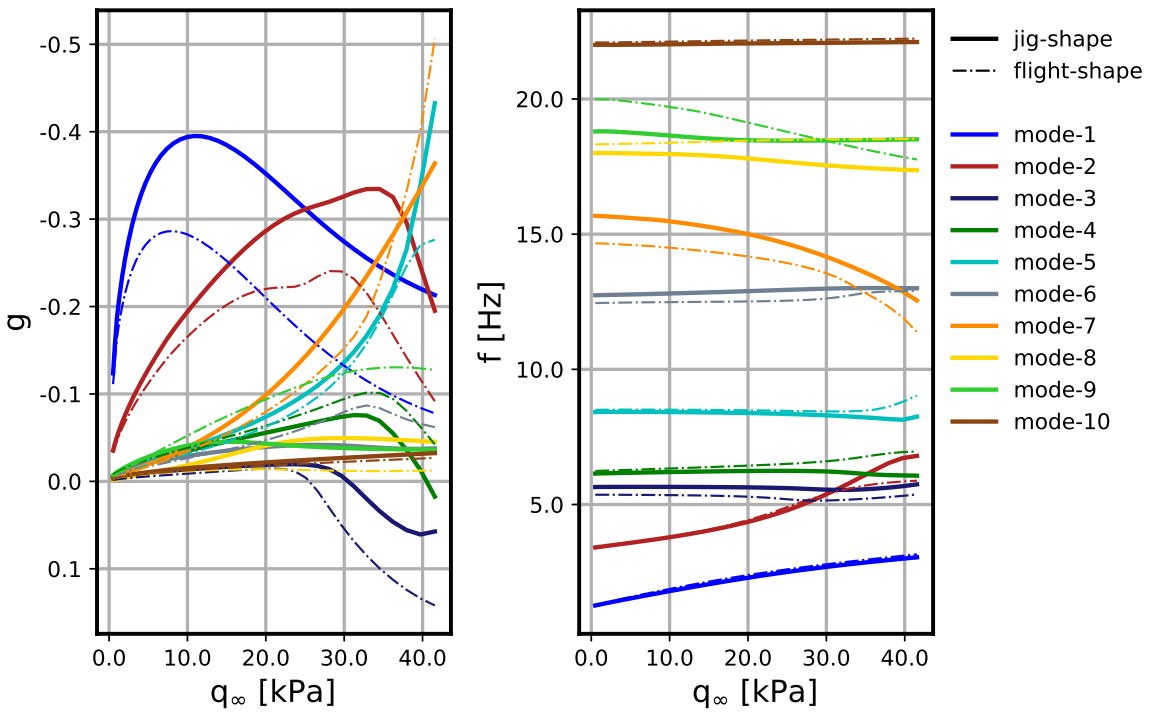

Figure 11: Damping and frequency trends for jig- and flight-shape configuration.

Table 4: Flutter boundaries for the three case studies.

	jig-shape		**flight-shape**	**pre-loaded**
	mode-3	mode-4	mode-3	mode-3
$q_{\infty,f}$[kPa]	30.4	40.5	25.5	26.1
$k_{red,f}$[−]	0.150	0.141	0.153	0.152
f_f[Hz]	5.542	6.064	5.170	5.152

Figure 12 shows the shape of the unstable aeroelastic mode-3 for the jig- and flight-shape at $q_\infty = q_{\infty,f}$. The complex amplitude ratio of the individual structural eigenmodes for flutter mode-3 is listed in Table 5. One can see that in the jig-shape study mode-1, mode-2 and mode-4 interact mainly, which can also be seen in Figure 12 by the second order wing bending. In case of the flight-shape, mode-2 dominates and a coupling with mode-1 and mode-3 appears.

These three dominating modes are used to compare the $\bar{Q}_{hh}$ elements, which are illustrated in Figure 13. It is noticeable that the imaginary parts have close similarities. For the real part, larger deviations can be observed. By considering the pressure distributions in Figure 9, this seems reasonable, since the lift distribution has changed significantly.

Table 5: Modal amplitude ratios of participating structural eigenmodes for flutter mode-3 and $q_\infty = q_{\infty,f}$.

structural mode:	1	2	3	4	5	6	7	8	9	10
jig-shape:	0.282	0.318	0.116	0.191	0.023	0.002	0.029	0.009	0.017	0.009
flight-shape:	0.330	0.343	0.157	0.088	0.021	0.005	0.028	0.001	0.018	0.004

(a) jig-shape flutter mode-3

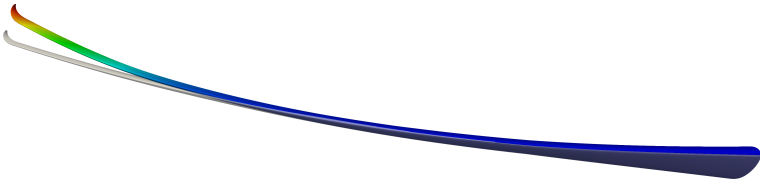

(b) flight-shape flutter mode-3

Figure 12: Displacement results of the flutter modes, scaled to $|\delta u| = 1\,\mathrm{m}$.

5 CONCLUSION

In this work, the influences of a pre-loaded wing structure on the flutter characteristic are investigated. Therefore, an aeroelastic modeling process to describe an elastic wing structure in jig- and flight-shape is presented. To predict the flutter instability, the aeroelastic equation is solved by means of the p-k method. The unsteady aerodynamic forces in the transonic flight regime were described with the RANS equations in the time domain and solved using CFD methods.

To analyze the physical influences separately, three aeroelastic models were presented. As starting model, a wing in jig-shape was used, which was brought into a trimmed cruise flight condition at $Ma = 0.8$ in $FL = 330$. To study the influences of pre-loading, the wing model was first brought into flight-shape with updating its geometry and reassembly of the structural stiffness and mass matrix. A third model was assembled by using the structural stiffness and mass matrix of the previous trim calculation, so that the load history and thus stress-stiffening effects are included.

Differences between jig- and flight-shape models were first studied individually on the structural and aerodynamic field. The changed modal mass and stiffness distribution of the wing in flight-shape already lead to a notable different modal behavior. Between the flight-shape and pre-loaded wing model, only minor differences could be observed. The reassembly of mass and stiffness matrix in flight-shape, based on the updated geometry, showed to cover most dominating effects. The study showed that stress-stiffening has no considerable effect at lower load factors. On the aerodynamic side, a significant change in the lift distribution could be observed, which is mainly caused by the wing washout.

In the aeroelastic simulations those influences lead to different critical flutter pressures. The change in lift distribution between jig- and flight-shape could also be observed in the unsteady aerodynamic forces. While the phase shift shows a high similarity, the changed lift distribution is observable in the force magnitudes.

The presented study was simplified to symmetric boundary conditions and exclusion of rigid-body modes, so that not all physical effects necessary for the complete description of an aircraft are covered. Yet it was shown that for the presented exemplary wing, important changes in the aeroelastic behaviour occur. The largest influence was identified by the simple geometrical change from jig- to flight-shape, which is why consequently the flight-shape should be used for the aeroelastic design and evaluations.

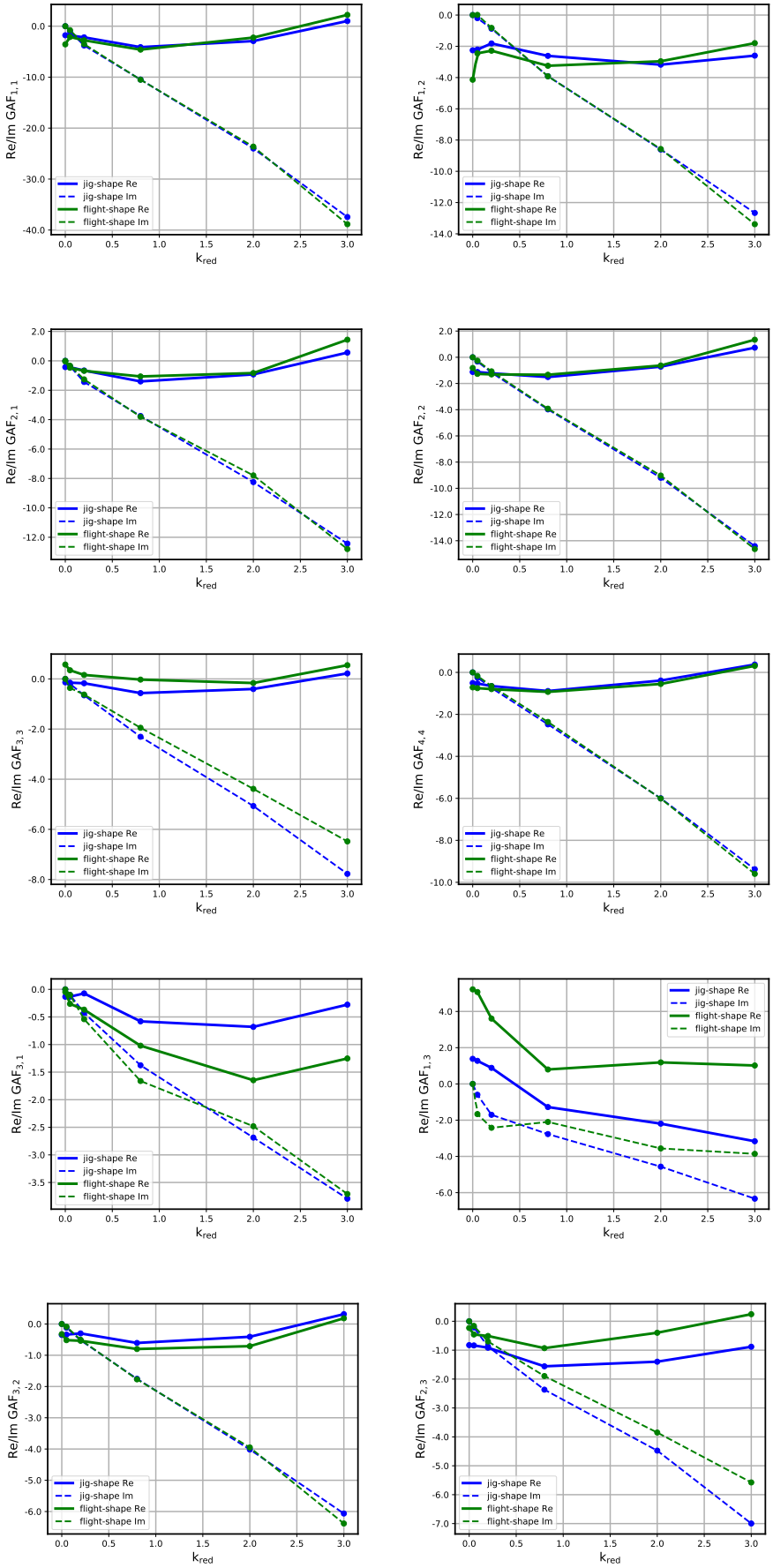

Figure 13: Jig- to flight-shape comparison of the resulting $\bar{Q}_{hh}$ entries of the dominant flutter modes.

6 REFERENCES

[1] Scheelhaase, J., Grimme, W., O'Sullivan, M., et al. (2018). Klimaschutz im Verkehrssektor; Aktuelle Beispiele aus der Verkehrsforschung. *Wirtschaftsdienst*, 98(9), 655–663. ISSN 1613-978X. doi:10.1007/s10273-018-2347-y.

[2] FLEXOP Consortium (2015). Flutter Free Flight Envelope Expansion for Economical Performance Improvement. `https://flexop.eu`. Accessed: 2018-02-06.

[3] NASA - Air Force Research Laboratory (2015). X56A Multi-Utility Technology Testbed. `nasa.gov/centers/armstrong/research/X-56/index.html`. Accessed: 2018-02-06.

[4] R. Palacios, E. R., C. Cesnik (2007). Re-Examined Structural Design Procedures for very Flexible Aircraft. *IFASD*.

[5] V. Rozov, e. a. (2019). CFD-Based Aeroelastic Sensitivity Study of a Low-Speed Flutter Demonstrator. *aerospace*.

[6] Y. Harmin, J. C. (2010). Efficient Prediction of Aeroelastic Behaviour Including Geometric Non-Linearities. *51th AIAA Structures, Structural Dynamics, and Materials Conference*.

[7] M. Breuer, e. a. (2012). Fluid–Structure Interaction Using a Partitioned Semi-Implicit Predictor–Corrector Coupling Scheme for the Application of Large-Eddy Simulation. *Journal of Fluids and Structures*.

[8] Bonet, J. (2008). *Nonlinear Continuum Mechanics for Finite Element Analysis*. Camridge, United Kingdom: Cambridge University Press.

[9] P. Spalart, S. A. (1992). A One-Equation Turbulence Model for Aerodynamic Flows. *30th AIAA Aerospac Science Meeting*.

[10] C. Farhat, M. L. (1998). Load and Motion Transfer Algorithms for Fluid/Structure Interaction Problems with Non-Matching Discrete Interface: Momentum and Energy Conservation, Optimal Discretization and Application to Aeroelasticity. *Computer Methods and Applied Mechanical Engineering*.

[11] Freymann, R. (2011). *Strukturdynamik*. Springer-Verlag Berlin Heidelberg.

[12] Fleischer, D. (2014). Verfahren reduzierter Ordnung zur Ermittlung instationaerer Luftkraefte. *Dissertation Technische Universitaet Muenchen*.

[13] Rodden W.P., H. R. (1997). Aeroelastic Addition to NASTRAN. Tech. Rep. TR-3094, NASA.

[14] A. Hermanutz, M. H. (2017). High Fidelity Trim Calculation Under Consideration of Aeroelastic Effects of a High Aspect Ratio Swept Wing. *IFASD*.

[15] M. Kotzek, A. S. (2015). Modeling and Control for a Blended Wing Body Aircraft. *Springer-International*.

[16] MSC (2018). *Release Guide*. Newport Beach, CA, United States: MSC/Software Corporation.

COPYRIGHT STATEMENT